

Electron emission from particles strongly affects the electron energy distribution in dusty plasmas

Austin Woodard, Kamran Shojaei, Carla Berrospe-Rodriguez, Giorgio Nava, and Lorenzo Mangolini

Citation: *Journal of Vacuum Science & Technology A* **38**, 023005 (2020); doi: 10.1116/1.5134706

View online: <https://doi.org/10.1116/1.5134706>

View Table of Contents: <https://avs.scitation.org/toc/jva/38/2>

Published by the [American Vacuum Society](#)

A dark blue banner for AVS Quantum Science. The top left corner features a green diagonal banner with the word "NEW" in white. The background is decorated with various circular icons representing quantum science concepts, such as atomic models, wave patterns, and circuitry. The main text "AVS Quantum Science" is in large white font. Below it, the tagline "A new interdisciplinary home for impactful quantum science research and reviews" is in smaller white font. In the bottom left, it says "Co-Published by" above the AIP Publishing and AVS logos. In the bottom right, a green button contains the text "NOW ONLINE".

NEW

AVS Quantum Science

A new interdisciplinary home for impactful quantum science research and reviews

Co-Published by

AIP Publishing AVS

NOW ONLINE

Electron emission from particles strongly affects the electron energy distribution in dusty plasmas

Cite as: J. Vac. Sci. Technol. A **38**, 023005 (2020); doi: [10.1116/1.5134706](https://doi.org/10.1116/1.5134706)

Submitted: 1 November 2019 · Accepted: 3 January 2020 ·

Published Online: 27 January 2020



Austin Woodard,^{1,a)} Kamran Shojaei,^{2,a)} Carla Berrospe-Rodriguez,²  Giorgio Nava,²  and Lorenzo Mangolini^{1,2,b)} 

AFFILIATIONS

¹Materials Science and Engineering Program, University of California Riverside, Riverside, California 92521

²Department of Mechanical Engineering, University of California Riverside, Riverside, California 92521

Note: This paper is part of the Special Topic Collection Commemorating the Career of John Coburn.

a)Contributions: A. Woodard and K. Shojaei contributed equally to this work.

b)Electronic mail: lmangolini@engr.ucr.edu

ABSTRACT

The electron energy distribution of a low-temperature dusty plasma has been measured via a Langmuir probe. An unexpected broad peak at energy in the 2–4 V range has been observed. This can be theoretically reproduced for a sufficiently large electron emission rate from the nanoparticles dispersed in the plasma. A careful analysis of the nanoparticle energy balance, using measured values of nanoparticle concentration and plasma density, confirms that particles are sufficiently hot under the conditions of this study to rapidly inject electrons into the plasma via field-assisted thermionic emission. This work suggests that the presence of dust affects the plasma ionization balance more deeply than previously thought.

Published under license by AVS. <https://doi.org/10.1116/1.5134706>

I. INTRODUCTION

Low-pressure, low-temperature nonthermal dusty plasmas are weakly ionized gases containing particulate of condensed matter. They are ubiquitous in industrial and academic plasma laboratories. The formation of dust in industrial processing plasmas was initially treated as a source of contamination.^{1,2} That view has progressively evolved to one in which plasmas are a viable and controllable route for nanopowder fabrication. Despite many promising reports confirming the potential of plasma-produced nanoparticles,^{3–10} an increased understanding of the fundamental physics of dusty plasmas is in our opinion necessary to further advance this field. In particular, the mutual interaction between the plasma and the nanoparticles dispersed within it is far from being fully understood, a problem exacerbated by the fact that this is a notoriously difficult system to probe experimentally. While it is accepted that the recombination of plasma-produced species at the surface of the nanoparticles can induce heating and crystallization of even high melting point materials,^{7,11–13} its complementary aspect, i.e., how the presence of particles affects the plasma, has received significantly less attention. The current understanding is that particles suspended in a plasma effectively behave as electron sinks, draining electrons from the discharge and hence becoming unipolarly negatively charged.

This effect induces a reduction of the plasma electron density and, correspondingly, an increase in the electron temperature to support the discharge ionization balance. Their large attachment cross section depletes the electron energy distributions at potentials higher than the nanoparticle floating potential.

In this contribution, we show that the presence of nanoparticles has more profound effects than previously expected. Using a Langmuir probe, we have found that a large fraction of the electron population has energies 2–3 eV above the plasma potential. A theoretical solution of the electron energy distribution function suggests that electrons are ejected from the nanoparticles via electron emission and injected into the plasma with an energy corresponding to the nanoparticle floating potential. In other words, nanoparticles behave as distributed electron emitters. The nanoparticle charge balance is solved by accounting for several mechanisms, including photoelectric emission, secondary emission due to the impact of charged species at the particles' surface, thermionic emission, and electron evaporation due to the negative charge already present on the particle. Coupled with the solution of the nanoparticle energy balance, this approach allows us to conclude that both plasma-induced heating (i.e., thermionic emission) and a reduced barrier for electron evaporation (i.e., field-assisted emission) are the main

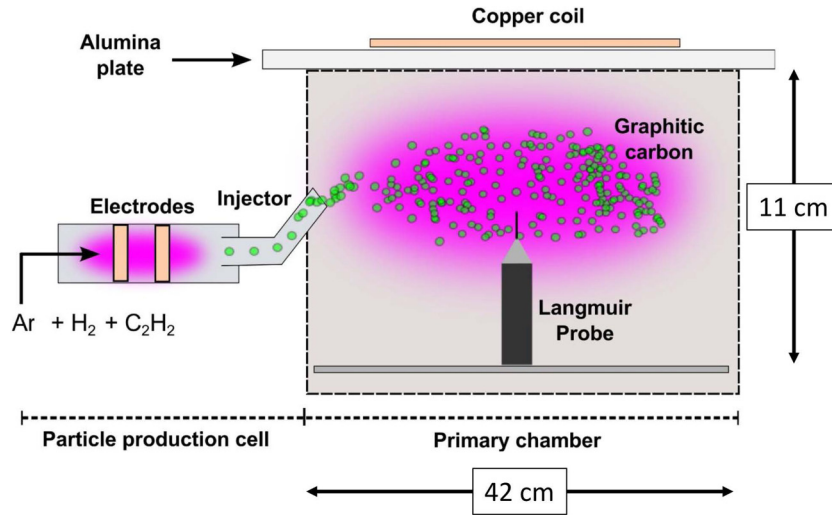


FIG. 1. Schematic of the two-stage system used in the experiments. The gas flow was a mixture of 30 SCCM Ar, 1.5 SCCM H₂, and 3 SCCM C₂H₂, with a pressure differential of 1.5 Torr:15 mTorr in the particle production cell and primary chamber maintained by a 2 mm orifice. In both reactors, independently controlled radio frequency (13.56 MHz) generators are connected to L-type matching networks to maintain the discharge.

mechanisms contributing to the injection of electrons from the particles into the plasma. Overall, this is the first report of the direct measurement of the nanoparticle floating potential, and corresponding charge, in a nonthermal plasma.

John Coburn pioneered experiments designed to understand how plasmas and surfaces interact and influence each other. When he was active, materials and surfaces of interest were mostly silicon wafers, films on silicon wafers, and reactor walls. Our work continues the investigation of the interaction between plasmas and surfaces, this time focusing on nanoparticles in plasma.

II. EXPERIMENT

A. Experimental setup

A schematic of the experimental setup is reported in Fig. 1. The experiments were performed in a vacuum chamber equipped with an inductive planar coil radio frequency (RF) source for plasma generation and a Langmuir probe for the measurement of the discharge properties.¹⁴ This primary chamber is dosed with carbon nanoparticles produced from the dissociation of acetylene (C₂H₂) in an auxiliary plasma, the particle production cell. More details about the working principle of the system are detailed in our previous publication.¹⁵ The RF power in the production cell is maintained at 100 W, while the power in the primary chamber ranged from 60 to 120 W. Full consumption of C₂H₂ in the particle production cell was verified with a residual gas analyzer measurement. The nanoparticle injection rate in the primary chamber was carefully measured with a gravimetric method. A stainless-steel mesh was attached at the exit of the injection tube to capture the carbonaceous particles produced by the production cell. The injection rate was calculated from the total collected mass (measured with a Sartorius ENTRIS64-1S microbalance).

B. Optical measurement of particle density

In order to estimate the particle density in the primary chamber, laser scattering intensity measurements were performed in the system (see Fig. 2).

A continuous wave laser of $\lambda = 532$ nm, a spot size of $500 \mu\text{m}$, and a laser power of $P = 1.5$ W was introduced in one of the window ports of the primary chamber. The Rayleigh scattered light from graphitic carbon nanoparticles was collected in a 90° configuration from a second port of the primary chamber. A linear polarizer was located right after the collection window to reduce the laser light noise produced by the scattered reflections of the stainless-steel chamber's interior. The scattered light from the graphitic particles was focused into a multimode glass fiber with an air-spaced doublet collimator (Thorlabs), connected to a triple grating imaging spectrometer (Acton Spectra Pro, Princeton Instruments). The inlet grating from the monochromator was close to $30 \mu\text{m}$ width to obtain high-resolution spectra and differentiate scattered laser light from the Ar–H₂ plasma emission spectrum. The emission spectra were captured by a CCD camera (1024×256) located at the exit monochromator's slit, with an acquisition time of 250 ms and a total recording of 300 frames. The spectrometer was connected to a computer to visualize and record the emission spectrum. The Rayleigh scattering measurements were performed under an internal total pressure of 20 mTorr, a mass flow rate of 30 SCCM Ar, 1.5 SCCM H₂, and 3 SCCM of C₂H₂ with RF power sweep from 20 to 120 W, in steps of 20 W. The scattered signal intensity from the graphitic particles I_p , trapped in the main chamber, was calculated as

$$I_p = I_{lpp} - (I_l + I_{pp}), \quad (1)$$

where I_l is the background intensity of the laser collected in the absence of particles and trapping plasma (i.e., only argon and hydrogen gases were flowing in the chamber); I_{lpp} is the scattered light intensity in the presence of laser, particles, and the Ar–H₂ trapping plasma; and I_{pp} is the intensity of the plasma emission with particles flowing in the absence of the laser. Equation (1) was hence used to obtain a quantitative measurement of the Rayleigh intensity peak of the particles, I_p , subtracting the plasma emission and laser background contributions. The emission spectra of I_b , I_{lpp} , and I_{pp} are shown in Fig. 2(b).

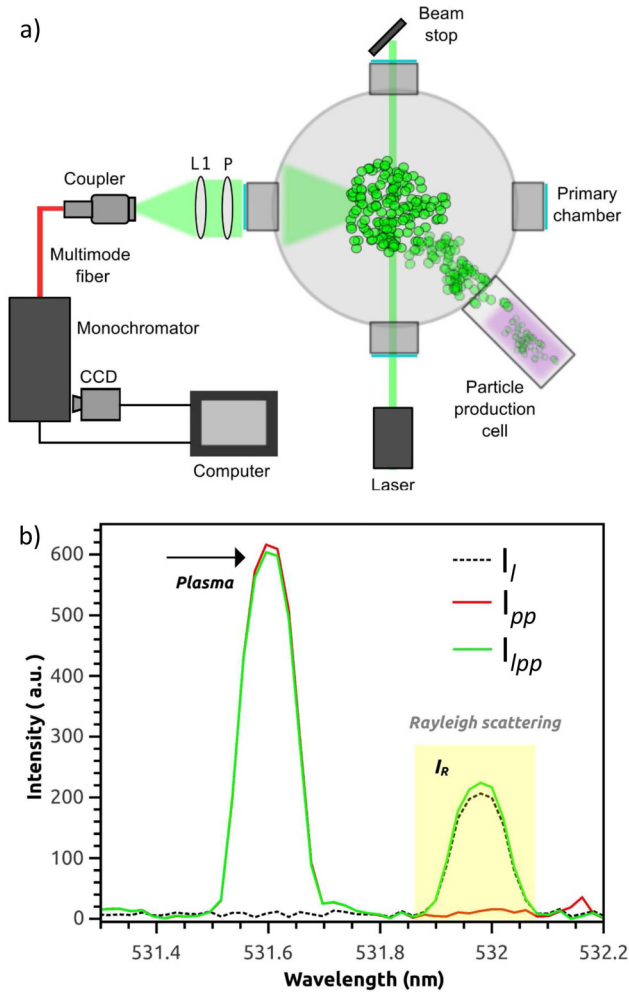


FIG. 2. Schematic of the setup employed for the measurement of the Rayleigh scattering from the carbon particles suspended in the primary plasma (a). A 532 laser (500 mW power) enters the primary chamber through a highly transmitting viewport. The Rayleigh scattering is collected from a second viewport (b) in a 90° configuration.

Theoretically, the Rayleigh scattering intensity is defined as $I_p = I_o \cdot n_p \cdot \sigma_p$, where I_o is the incident intensity of the laser, n_p is the particle density, and σ_p is the scattering cross section of the carbon particles, which can be defined as¹⁶

$$\sigma_p = \frac{2\pi^5}{3} \left| \frac{m^2 - 1}{m^2 + 1} \right|^2 \frac{(2R)^6}{\lambda^4}, \quad (2)$$

where R is the radius of the particles, λ is the wavelength of the scattered light, and m is the complex refractive index of carbon $m = n + ik$, with $n = 1.915$ and $k = 0.952$, where n represents the refractive index and k represents the extinction coefficient of the material. We carried out measurements of the scattered light intensity

for argon at a pressure of 1 atm to calibrate the response of our detection system, i.e., to perform a relative measurement of the scattering intensity with respect of a known scattering medium. The resulting scattering intensity is $I_G = I_o \cdot n_{Ar} \cdot \sigma_{Ar}$, with $n_{Ar} = 2.69 \times 10^{19} \text{ cm}^{-3}$ being the argon number density, as calculated using the ideal gas law, and $\sigma_{Ar} = 4.45 \times 10^{-27} \text{ cm}^2$ being the scattering cross section from argon.¹⁷ The particle density n_p can then be calculated as

$$n_p = \frac{I_p \cdot n_{Ar} \cdot \sigma_{Ar}}{I_G \cdot \sigma_p}. \quad (3)$$

It is important to mention that, in the described analysis of the light scattering signal, we assumed the particles to be isolated and non-interacting spheres. We expect this to be a valid assumption for the case of nanoparticles that are electrostatically stabilized in the plasma.

III. RESULTS AND DISCUSSION

The primary plasma of the setup was dosed with graphitic carbon nanoparticles produced in an auxiliary RF discharge placed at the inlet of the primary chamber. This particle generation cell fully consumes acetylene and converts it into the graphitic particles as shown in the inset of Fig. 3(a).^{15,18} This two-stage reactor allows investigating the influence of nanoparticles on the plasma properties by decoupling it from the nucleation and growth phase, which occurs in a spatially separated particle generation cell. As already described in our previous contribution, the use of conductive particles, such as the graphitic ones used here, prevents the formation of an insulating layer on the probe tip and enables its functionality in dust-rich discharges.^{19,20} An in-depth description of the setup, its working principle, the method, and the theory for obtaining the Langmuir probe measurements inside the dusty environment are detailed in our previous work.¹⁵

The particle size distribution for the graphitic carbon nanoparticles is shown in Fig. 3(a). The average particle size is 12 nm with a standard deviation of 3.8 nm. Raman analysis (Fig. S1)⁶⁰ confirms the highly graphitic structure of the particles. Figure 3(b) shows the electron energy probability functions (EPPFs), $f(\epsilon)$, measured in the primary chamber at varying input powers, with carbon nanoparticles injected in the plasma. The electron energy distribution functions (EEDFs), $F(\epsilon)$, were derived from the probe characteristics using the Druyvesteyn method.²¹ The EEPF $f(\epsilon)$ is defined as $F(\epsilon) \cdot \epsilon^{-1/2}$. The EPPFs show a broad peak in the 2–4 eV range with the peak position varying smoothly and increasing with increasing input power. Peaks in the EEPF have been reported in afterglow discharges, in the high-energy tail of the distribution because of the latent Penning ionization.²² However, in this scenario, the peak in the electron energy does not vary with the process parameters since it is constrained by the metastable energy and ionization potential of the utilized gases. Our observation is clearly different. We measure a shift as a function of RF power, with exactly the same gas composition. Moreover, we have never observed the peak under pristine conditions, i.e., without particles. This strongly suggests that the peak in the EEPFs is correlated with the presence of particles in the plasma.

It is also interesting to point out that the potential range in which the peak is observed, 2–3 V below the plasma potential, is strikingly close to the expected nanoparticle floating potential for

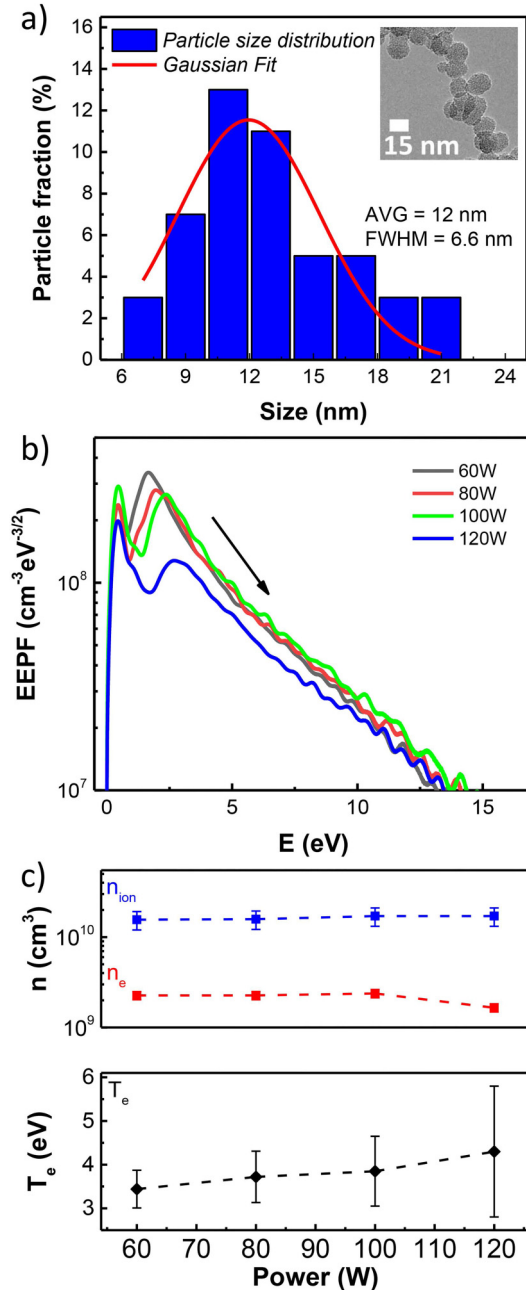


FIG. 3. Particle size distribution measured from TEM analysis and fitted with a Gaussian profile (a). The inset shows a TEM micrograph of the synthesized particles. Measured EEPF (b), n_e , n_{ion} , and T_e as a function of the input plasma power (c).

this type of low-pressure discharges, as predicted by the orbital motion limited (OML) theory. Electrons ejected from a negatively charged particle will gain energy equal to the floating potential as they cross the sheath and enter the plasma. To validate this

hypothesis, we first proceed to measure the nanoparticle charge in the plasma volume by measuring the deficit between ion and electron densities. Under the assumption of quasineutrality, the average charge per particle Q can be calculated using the following equation:

$$n_e = n_{ion} - Qn_p. \quad (4)$$

The ion and electron densities for the conditions under consideration are shown in Fig. 3(c). The ion density is obtained by fitting the IV probe characteristic, in the ion saturation regime, to the well-known $(V_{probe} - V_{plasma})^{1/2}$ dependence described by the OML theory. The electron density is obtained by integrating the measured EEDFs. For completeness, we also show the electron temperature T_e as a function of input power in Fig. 3(c). The nanoparticle density n_p has been measured using laser light scattering from a continuous wave 532 nm solid-state laser.

In Fig. 4(a), we show a photograph of the intense laser line, which can be distinguished even by the naked eye. Photographs of the laser beam at different times “ t ” are also shown in the same figure. Here, “ t ” is the time delay from when the plasma in the primary chamber is ignited. At $t = 0$, i.e., when the plasma has not been ignited yet, the scattering from the laser line is not visible. The scattering intensity increases after the plasma is ignited, stabilizes within a few minutes, and becomes clearly distinguishable even by the naked eye. This suggests that significant particle trapping is occurring, with the density of particles in the plasma slowly increasing to a steady state value. A 90° optical configuration was used to collect the scattered laser intensity, defined as $I_p = I_o \cdot n_p \cdot \sigma_p$, where I_o is the incident intensity of the laser, n_p is the particle density, and σ_p is the scattering cross section of a carbon particle.¹⁶ The value of n_p was then calculated from Eq. (3). A detailed description of the Rayleigh spectra processing is shown in Sec. II A. In the calculation, the effective Rayleigh scattering cross section σ_p was calculated by convoluting over the Gaussian fit of the particle size distribution in Fig. 3(a). This is necessary given the $(2R)^6$ dependence of the scattering cross section over the particle diameter $2R$.¹⁶ The particle density n_p as a function of plasma power of the primary chamber is shown in Fig. 4(b). We find a value of $\sim 2 \times 10^9 \text{ cm}^{-3}$, with no statistically meaningful dependence over plasma power. We have also measured the nanoparticle injection rate from the particle producing cell to the primary chamber. This has a value of 1.6 mg/h, from which we can estimate a nanoparticle density of $\sim 10^7 \text{ cm}^{-3}$ if no trapping was present. The fact that the scattering signal increases considerably when the primary plasma is ignited, and the fact that the measured nanoparticle density is significantly higher than what is predicted by the mass balance, confirms that nanoparticle trapping is relevant in this system and must be accounted for when calculating the average particle charge using Eq. (4).

In Fig. 4(c), we show the particle charge calculated according to two different approaches. In the first, the average particle charge was calculated using Eq. (4) from the quasineutrality condition. The average charge has a weak dependence on power, with a value between six and seven elementary charges per particle. This is in reasonable agreement with theoretical predictions, although we point out that the error bar in this measurement is significant. At 120 W of input power, Q is expected to be in the broad range between 4 and 11 charges per particle. This is a consequence of

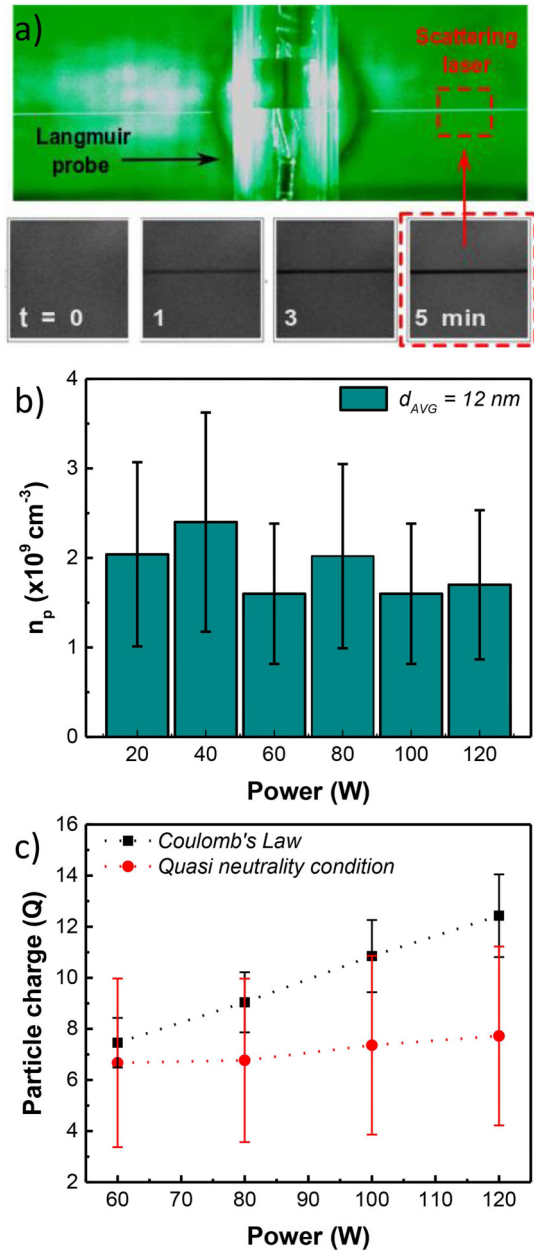


FIG. 4. Picture showing the laser scattering from the graphitic carbon particles injected in the primary chamber (a). The inset shows an image sequence of the scattering line as a function of time, highlighting the building up of the particle-trapping phenomenon. Trapped nanoparticle density as a function of plasma power (b). Absolute value of the particle charge as a function of the applied RF power calculated from the plasma charge deficit and the particle potential (c).

cumulative errors in the measurement of ion and electron densities, and most importantly in the measurement of the nanoparticle density, with uncertainty in the scattering cross section being the dominant source of uncertainty [see Fig. 4(b)]. Estimating the

nanoparticle size via TEM is notoriously imprecise, and the sixth-power dependence of cross section over particle size amplifies the error in the determination of the optical cross section.

In Fig. 4(c), we also show the particle charge assuming that the peaks in the EEPFs shown in Fig. 3(b) are due to electrons emitted from the nanoparticles and that the peak position corresponds to the nanoparticle floating potential derived from Coulomb's law, $\Phi = Z_k / (4\pi \cdot \epsilon R)$, with $Z_k = Qe$ (where e is the electron charge, ϵ is the vacuum permittivity, and Q is number of elementary charges per particle). The results obtained via this approach are in reasonable agreement at low input power with a more significant deviation at higher power. The error bar for this measurement is also significantly smaller than when using quasi-neutrality, mainly because this method does not require the calculation of the laser scattering cross section. We also stress that we are neglecting any possible nanoparticle agglomeration effect in the plasma, which would lower the nanoparticle density and result in a larger charge when using Eq. (4).

The reasonable agreement between these two approaches to determining nanoparticle charge offers some partial validation to the hypothesis that the peak in the EEPF is due to the nanoparticles dispersed in the plasma. Additional validation is provided next by discussing a self-consistent model for the theoretical prediction of the EEPF in dusty plasmas, accounting for the electron emission effect from the dust. The model is based on the freeware software Bolos, which provides a solution of energy probability function via a two-term approximation of the Boltzmann transport equation under steady state.^{23,24} This solver requires as an input the reduced electric field E/N ; the gas-phase composition in terms of argon, hydrogen, and nanoparticle densities; and the appropriate collision cross sections. We stress that the collision cross sections for the particles strongly depend on their floating potential. The cross sections for elastic and inelastic processes for argon and hydrogen are taken from the LxCat database.²⁵ For the nanoparticles, the elastic cross section is determined by a Coulomb scattering process and has the following expression:²⁶

$$\sigma_{\text{elastic}}(\Phi, E) = 2\pi R^2 \left(\frac{\Phi}{E}\right)^2 \log \left(\frac{\lambda_{LD}^2 + \left(\frac{\Phi}{2E}\right)^2 R^2}{\left(1 + \frac{\Phi}{E}\right) R^2 + \left(\frac{\Phi}{2E}\right)^2 R^2} \right), \quad (5)$$

where λ_{LD} is the linearized Debye length, which is defined as follows:

$$\frac{1}{\lambda_{LD}} = \frac{1}{\lambda_{De}} + \frac{1}{\lambda_{Di}} + \frac{1}{\lambda_p}, \quad (6)$$

$$\lambda_{De} = \sqrt{\frac{\epsilon k_B T_e}{e^2 n_e}}, \quad \lambda_{Di} = \sqrt{\frac{\epsilon k_B T_{ion}}{e^2 n_{ion}}}, \quad \lambda_{Dp} = \sqrt{\frac{\epsilon k_B T_{pe}}{e^2 n_p}}, \quad (7)$$

where λ_{De} , λ_{Di} , and λ_p are electron, ion, and particle Debye lengths; E is the electron kinetic energy; k_B is the Boltzmann constant, T_{ion} is the ion temperature, and T_{pe} is the translational temperature of the particles, assumed to be 300 K. The attachment cross section (i.e., for

electrons being collected by the particles) is zero for energies below the nanoparticle floating potential since electrons cannot overcome the potential barrier induced by the nanoparticle negative charge. For energies higher than the floating potential, we used the expression from Ref. 26. The resulting cross section is then

$$\sigma_{coll} = \begin{cases} \pi R^2 \left(1 + \frac{\Phi}{E}\right), & E > -\Phi, \\ 0, & E \leq -\Phi. \end{cases} \quad (8)$$

Finally, we account for the electron emission from the nanoparticles by introducing a detachment cross section with the following expression:

$$\sigma_{detach} = \frac{b}{\sqrt{\pi}} \exp \left[-\left(\frac{E - |\Phi|}{a} \right)^2 \right]. \quad (9)$$

This expression effectively treats the electron detachment cross section as a delta function, i.e., electrons are emitted from the nanoparticles with an energy corresponding to their floating potential Φ . The Gaussian profile is centered at the nanoparticle floating potential and its width a is small and equal to 0.045 eV, to approximate the cross section to a delta function. The solution is not dependent on the choice of a in the limit of a narrow width. In principle, varying the width of the cross section could be used to account for charge distribution effects. We leave a more focused investigation on this aspect for a future contribution. The parameter b is used to arbitrarily scale the magnitude of the detachment cross section and consequently to vary the rate of electron emission from the nanoparticles (i.e., from no electron emission to fast electron emission). Computationally, we have found that the most effective way to account for detachment in the Boltzmann solver Bolos is to treat the cross section as a “negative” attachment cross section, i.e., not to remove but to introduce electrons at a specified energy equal to the floating potential Φ .

The ion collection frequency ν_{ion} , i.e., the frequency with which ions deposit positive charge onto the nanoparticle, is calculated from the OML theory assuming that H_3^+ is the dominant ion, as verified in our previous contribution,¹⁵

$$\nu_{ion} = 4\pi R^2 n_{ion} \sqrt{\frac{k_B T_{ion}}{2\pi m_{ion}}} \left(1 - \frac{e\Phi}{k_B T_{ion}} \right). \quad (10)$$

The electron attachment and detachment frequencies (ν_{attach} and ν_{detach} , respectively) are calculated using the respective cross sections and by averaging over the electron energy distribution function obtained by the Boltzmann solver. At steady state, Kirchhoff's law constraints the charge collection frequencies to

$$\nu_{ion} + \nu_{e-detach} = \nu_{e-attach}. \quad (11)$$

We introduce a detachment proportionality factor δ defined as

$$\nu_{e-detach} = \delta \nu_{ion}. \quad (12)$$

The Boltzmann transport equation is iteratively solved with Kirchhoff's law and the quasineutrality equation until convergence is reached. More specifically, the ion and electron densities are kept constant, and an EEPF based on an initial guess of Φ and n_p is generated. The corresponding collision cross sections are calculated using Eqs. (5), (8), and (9). The electron attachment and detachment frequencies are obtained by averaging over the initial guess of the EEPF. A new particle floating potential Φ is then calculated so that the ion collection frequency satisfies Kirchhoff's law via Eq. (11). The corresponding nanoparticle charge Q is calculated, and the nanoparticle density is updated using quasineutrality via Eq. (1). At this point, one iteration is completed. The cross sections for electron attachment and detachment are updated with the new value of Φ , and the gas-phase composition is updated using the new value of nanoparticle density. The process is repeated until the nanoparticle floating potential reaches convergence. Upon convergence, the model returns the electron energy distribution and probability functions (EEDF and EEPF), the nanoparticle floating potential Φ , and the particle density n_p . The amplitude of the detachment cross section b , and consequently the proportionality factor δ , is a free parameter varied from 0 (meaning no electron emission) to any arbitrary value to investigate the effect of electron emission on both the shape of the EEPF and on the nanoparticle charge.

Figure 5 shows the results obtained using the theoretical framework described above. In Fig. 5(a), we show the electron energy probability functions (EEPFs) calculated for different values of the electron emission proportionality factor δ and for the constant E/N equal to 70 T_d . δ is varied between 0 and 0.95. For the case of $\delta = 0$, no peak is distinguishable in the EEPF, as expected. Increasing values of δ lead to the appearance of a peak between 1 and 2 eV above the plasma potential. This feature becomes more pronounced for increasing values of δ . The peak position in the EEPF, which corresponds to the nanoparticle floating potential, decreases for increasing values of electron emission rate. This is expected, since the increased electron emission rate leads to a reduction in the steady state nanoparticle charge. In Fig. 5(b), we show the results of a parametric study in which the ion density is constant and equal to $2 \times 10^{10} \text{ cm}^{-3}$ and the electron density is varied between $1.75 \times 10^9 \text{ cm}^{-3}$ and $3.5 \times 10^9 \text{ cm}^{-3}$.

The particle charge predicted by our model and calculated from the floating potential is shown for different values of the electron emission proportionality factor δ , and it is also compared to that predicted by the OML theory. The particle charges obtained when $\delta = 0$ are in good agreement with the OML theory. As expected, with increasing δ values, the number of charges per particle decreases significantly compared to the OML theory. Overall, this model supports the hypothesis that a peak in the EEPF emerges due to the presence of dust in the discharge volume and can be tied to the injection of electrons in the plasma with kinetic energies equivalent to the floating potential.

Next, we discuss the physical mechanism giving rise to the efficient emission of electrons from the nanoparticles. First, we consider emission processes such as photodetachment or secondary emission due to electron or ion impact. For the case of photodetachment, a flux of photons with energies higher than the nanoparticle work function (5.1 eV for the case of carbon) can result in electron ejection from the surface.^{27,28} For the argon-hydrogen mixture used in

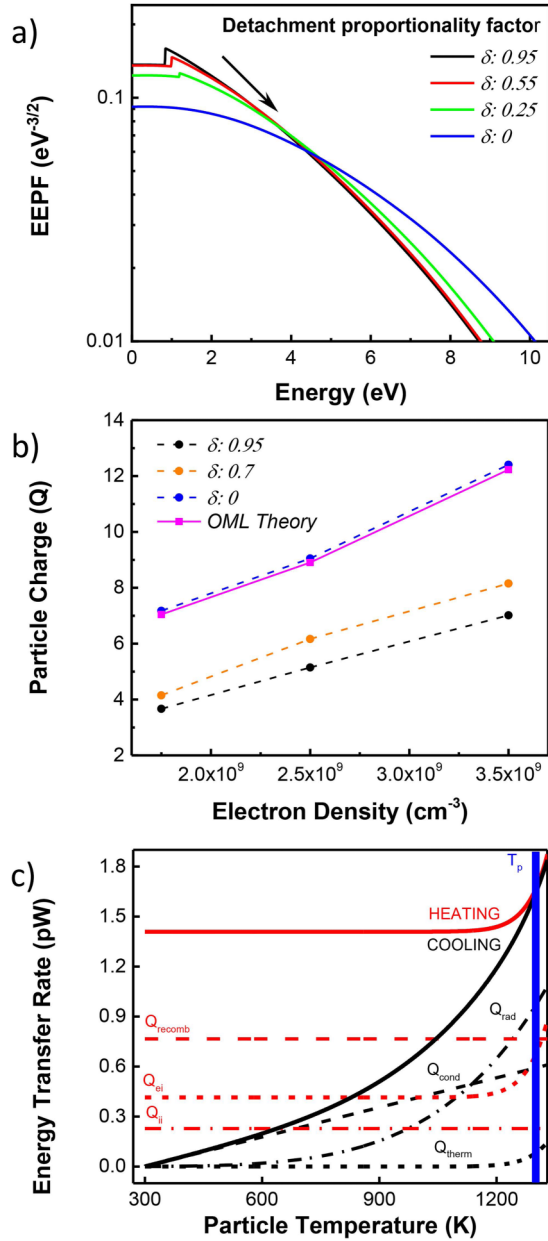


FIG. 5. (a) EEPFs calculated for different values of electron emission parameter. (b) Absolute value of the particle charge as a function of electron density as predicted by the OML theory and for increasing values of the electron emission parameter. (c) Nanoparticle heating and cooling rates. The intersection between the solid red line (cumulative heating) and the solid black line (cumulative cooling) is the nanoparticle temperature T_p .

our study, the main source of radiation with sufficient energy to induce photoemission are the two argon resonant lines at energies of 11.62 and 11.82 eV. We have followed the procedure outlined in Refs. 29–31 to estimate the photodetachment frequency. Briefly, we

have used a corona model and well-established values of excitation cross section to estimate the density of argon excited states, accounting for the radiation reabsorption probability, and assuming an electron emission yield of 100% per incident high-energy photon.^{32–37} With these assumptions, we find that the electron emission current from the particle due to photodetachment is <3% of the ion current to the particle. Therefore, for the conditions under consideration here, photoemission cannot be a significant contributor to a large electron emission.

Similarly, secondary electron emission resulting from the flux of charged species to the particle surface is not sufficient to justify the large electron current from the particles. As suggested by Chow *et al.*,^{38,39} electrons impinging with energies less than 10 eV cannot excite many secondary electrons or tunnel through the grain. Ion impact can induce the emission of a secondary electron via Auger neutralization. The number of secondary electrons created per incident ion is expressed as⁴⁰

$$\gamma \cong 0.016(E_{\text{inz}} - E_W) \cong 0, \quad (13)$$

where E_{inz} is the ionization potential of the hydrogen atom and E_W is the work function of graphitic nanoparticle (5.1 eV). Again, the yield is only a few percent in magnitude.

Finally, we consider the possibility that the particles may be sufficiently hot to rapidly lose electrons via thermionic emission. It is accepted that nanoparticles in nonthermal plasmas are heated well above the background gas temperature because of the recombination of plasma-produced species onto their surfaces.^{41–43} Here, we consider the possibility that this heating mechanism might actually have a large effect on the nanoparticle steady state charge. To investigate this, we also account for the effect of nanoparticle charge on the rate with which electrons are emitted from the surface (i.e., a field-assisted effect). We consider the following nanoparticle energy balance:

$$Q_{\text{cond}} + Q_{\text{rad}} + Q_{\text{therm}} = Q_{\text{ei}} + Q_{\text{ion}} + Q_{\text{rec}}. \quad (14)$$

The left-hand side accounts for heat loss due to conduction to the background gas Q_{cond} , radiative cooling Q_{rad} , and electron evaporation due to thermionic emission Q_{therm} . The right-hand side includes the heat source terms due to the deposition of kinetic energy by electron and ion currents to the particles, Q_{ei} and Q_{ion} , respectively, and due to charge recombination Q_{rec} . The heat conduction loss mechanism can be described as

$$Q_{\text{cond}} = \pi R^2 \left(n_{\text{H}_2} \sqrt{\frac{8k_B T_{\text{gas}}}{\pi m_{\text{H}_2}}} + n_{\text{Ar}} \sqrt{\frac{8k_B T_{\text{gas}}}{\pi m_{\text{Ar}}}} \right) \frac{3}{2} k_B (T_p - T_{\text{gas}}), \quad (15)$$

where T_p is the particle temperature, m_{Ar} and m_{H_2} are the atomic mass of argon and hydrogen molecules, respectively, T_{gas} is the background gas temperature (assumed to be 300 K), and n_{Ar} and n_{H_2} are argon and hydrogen densities calculated from the ideal gas law, respectively. The heat loss due to radiation is calculated by accounting for the spectral dependence of emissivity in the Rayleigh regime $(2\pi R)/\lambda < 1$. The emissivity, e_λ , is a function of complex index of

refraction,^{44,45}

$$e_\lambda = \frac{4\pi(2R)}{\lambda} \frac{6w_m k_m}{(w_m^2 - k_m^2 + 2)^2 + 4w_m^2 k_m^2}. \quad (16)$$

A fit to measurements of the real and imaginary components of the index of refraction for graphite yields $m = w_m - k_m i$, with $w_m = 2.213 + 9.55 \times 10^3 \lambda$ and $k_m = 0.7528 + 1.265 \times 10^4 \lambda$.^{46–49} The radiative cooling rate is then obtained by integrating the Planck function over all wavelengths,

$$Q_{rad} = 4\pi R^2 \int_0^\infty e_\lambda \frac{2\pi h c^2}{\lambda^5 \left[\exp\left(\frac{hc}{\lambda k_B T_p}\right) - 1 \right]} d\lambda, \quad (17)$$

where c is the speed of light, h represents the Planck constant, and λ is the wavelength.⁵⁰ Thermal ejection of electrons from charged particles contributes to their cooling. The energy required to remove an electron from the bottom of the conduction band corresponds to the material work function with a correction term accounting for the interelectron repulsion energy, which facilitates the removal of electrons. This removal energy is described as

$$E_{rem} = W_{bulk-graphite} - \frac{e}{8\pi\epsilon} \frac{(2Q - 1)}{R}, \quad (18)$$

where $W_{bulk-graphite}$ is the work function of bulk graphite.^{51,52} The thermionic cooling rate for a negatively charged particle is then expressed based on the Richardson–Dushman approximation given by^{53–59}

$$Q_{therm} = \frac{4eE_{rem} m_e (2\pi R k_B T_p)^2}{h^3} \exp\left(-\frac{eE_{rem}}{k_B T_p}\right). \quad (19)$$

The kinetic energy of ions and electrons impinging onto the particle surface is transferred to the lattice and contributes to the heating process. The heating rate due to ion bombardment is described as

$$Q_{ion} = \nu_{ion} \left(\frac{1}{2} k_B T_e + |e\Phi| \right), \quad (20)$$

where ν_{ion} is the ion collection frequency. Each ion, upon being collected by the particle, has a kinetic energy equal to the sum of $1/2 k_B T_e$, based on the Bohm sheath criterion, and the floating potential Φ due to the Coulombic attraction between the positive ion and the negatively charged particle. The heating rate due to electron collection is equal to

$$Q_{ei} = \nu_e 2k_B T_e, \quad (21)$$

where ν_e is the electron collection frequency and $2k_B T_e$ is the mean kinetic energy lost per electron collected at the particle surface.⁴⁰ The recombination of H_3^+ ions at the particle surface is assumed to release an energy equivalent to the ionization potential of hydrogen E_{inz} (13.6 eV) increased by the bond energy of

the hydrogen molecule E_{diss} (4.52 eV) divided by 2. This accounts for the dissociative–associative sequence that results in the recombination of atomic hydrogen and the formation of one hydrogen molecule for every two H_3^+ ions that reach the surface.⁴¹ The resulting heating rate is then

$$Q_{rec} = \nu_{ion} e \left(E_{inz} + \frac{E_{diss}}{2} \right). \quad (22)$$

Using this approach, we find that for a particle with 12 charges and for an electron temperature of 4.1 eV, the particle temperature reaches 1300 K [see Fig. 5(c)] and $\delta \cong 1$, suggesting that electron emission significantly affects the nanoparticle charge balance. It is also important to stress when using a bulk work function value $W_{bulk-graphite}$ of 5.1 eV, the electron emission rate at 1300 K would be 0.1 s^{-1} , which is not sufficient to affect the particle charge balance. Accounting for the charged state of the particles via Eq. (18) lowers the removal energy E_{rem} to 2.75 eV, increasing the electron emission rate to $2.9 \times 10^5 \text{ s}^{-1}$ and greatly affecting the charge balance of the particle. Both thermal and electrostatic effects need to be accounted for to reproduce the behavior reported in this manuscript.

IV. SUMMARY AND CONCLUSIONS

In conclusion, we have performed careful measurements of the EEDF in a low-pressure dusty plasma and observed the appearance of a peak in the distributions. A self-consistent model has been developed to investigate how the presence of the particles affects the EEDF, in particular, to account for the emission of electrons from the nanoparticles. The good qualitative agreement between the measurements and the calculations supports the hypothesis that nanoparticles act as distributed electron emitters, leading to the appearance of a peak in the EEDF that corresponds to the nanoparticle floating potential. A simple nanoparticle energy balance confirms that particles are hot, mainly as a consequence of the poor heat loss to the background gas due to low pressure and to the inefficient radiative losses at small particle sizes. In addition, the highly charged state of these small particles substantially decreases the barrier for electron emission. The combination of thermal and electrostatic effects leads to a significant electron emission current, which affects not only the particle charge balance but also the electron energy distribution in the plasma. This work provides the first direct electrical measurement of the nanoparticle floating potential in a dusty plasma and represents a step toward understanding the complex coupling between plasmas and nanoparticles dispersed within it.

ACKNOWLEDGMENTS

This work was supported by the U.S. Department of Energy (DOE), Office of Science, Early Career Research Program under Award No. DESC0014169. Carla Berrospe acknowledges the support of the UC Mexus Postdoctoral Fellowship.

REFERENCES

- G. S. Selwyn, C. A. Weiss, F. Sequeda, and C. Huang, *J. Vac. Sci. Technol. A* **15**, 2023 (1997).
- G. S. Selwyn, J. Singh, and R. S. Bennett, *J. Vac. Sci. Technol. A* **7**, 2758 (1989).

- ³P. Firth and Z. C. Holman, *ACS Appl. Nano Mater.* **1**, 4351 (2018).
- ⁴T. Chen, K. V. Reich, N. J. Kramer, H. Fu, U. R. Kortshagen, and B. I. Shklovskii, *Nat. Mater.* **15**, 299 (2015).
- ⁵A. A. Barragan, G. Nava, N. J. Wagner, and L. Mangolini, *J. Vac. Sci. Technol. B* **36**, 011402 (2018).
- ⁶M. Sinha, A. Izadi, R. Anthony, and S. Roccabianca, *Nanoscale* **11**, 7520 (2019).
- ⁷S. Exarhos, A. Alvarez-Barragan, E. Aytan, A. A. Balandin, and L. Mangolini, *ACS Energy Lett.* **3**, 2349 (2018).
- ⁸A. A. Barragan, A. N. V. Ilawe, L. Zhong, B. M. Wong, and L. Mangolini, *J. Phys. Chem. C* **121**, 2316 (2017).
- ⁹G. Nava *et al.*, *J. Mater. Chem. C* **5**, 3725 (2017).
- ¹⁰G. Nava, F. Fumagalli, S. Neutzner, and F. Di Fonzo, *Nanotechnology* **29**, 465603 (2018).
- ¹¹A. A. Barragan, S. Hanukovich, K. Bozhilov, S. S. R. K. C. Yamijala, B. M. Wong, P. Christopher, and L. Mangolini, *J. Phys. Chem. C* **123**, 21796 (2019).
- ¹²T. Lopez and L. Mangolini, *J. Vac. Sci. Technol. B* **32**, 061802 (2014).
- ¹³K. S. Schramke, Y. Qin, J. T. Held, K. A. Mkhoyan, and U. R. Kortshagen, *ACS Appl. Nano Mater.* **1**, 2869 (2018).
- ¹⁴V. A. Godyak, R. B. Piejak, and B. M. Alexandrovich, *J. Appl. Phys.* **73**, 3657 (1993).
- ¹⁵A. Woodard, K. Shojaei, G. Nava, and L. Mangolini, *Plasma Sources Sci. Technol.* **27**, 104003 (2018).
- ¹⁶H. Moosmüller and W. P. Arnott, *J. Air Waste Manag. Assoc.* **59**, 1028 (2009).
- ¹⁷M. Snee and W. Ubachs, *J. Quant. Spectrosc. Radiat. Transf.* **92**, 293 (2005).
- ¹⁸A. Woodard, K. Shojaei, G. Nava, and L. Mangolini, *Plasmas Chem. Plasma Process.* **38**, 683 (2018).
- ¹⁹M. Klindworth, O. Arp, and A. Piel, *Rev. Sci. Instrum.* **78**, 033502 (2007).
- ²⁰N. Bilik, R. Anthony, B. A. Merritt, E. S. Aydil, and U. R. Kortshagen, *J. Phys. D Appl. Phys.* **48**, 105204 (2015).
- ²¹M. J. Druyvesteyn, *Z. Phys.* **64**, 781 (1930).
- ²²C. A. DeJoseph, Jr., V. I. Demidov, and A. A. Kudryavtsev, *Phys. Plasmas* **14**, 057101 (2007).
- ²³G. J. M. Hagelaar and L. C. Pitchford, *Plasma Sources Sci. Technol.* **14**, 722 (2005).
- ²⁴Bolos: Boltzmann equation solver open sources library, see: <https://github.com/aluque/bolos>
- ²⁵See: www.lxcat.net
- ²⁶S. A. Khrapak and G. E. Morfill, *Phys. Rev. E* **69**, 066411 (2004).
- ²⁷M. Rosenberg, D. A. Mendis, and D. P. Sheehan, *IEEE Trans. Plasma Sci.* **24**, 1422 (1996).
- ²⁸M. Rosenberg and D. A. Mendis, *IEEE Trans. Plasma Sci.* **23**, 177 (1995).
- ²⁹NIST Atomic Spectra Database, see: <https://physics.nist.gov/asd>
- ³⁰A. C. G. Mitchell and M. W. Zemansky, *Resonance Radiation and Excited Atoms* (Cambridge University, Cambridge, 1961).
- ³¹T. Holstein, *Phys. Rev.* **72**, 1212 (1947).
- ³²U. Kortshagen and L. D. Tsendin, *Electron Kinetics and Applications of Glow Discharges* (Springer, New York, 1998).
- ³³T. Holstein, *Phys. Rev.* **83**, 1159 (1951).
- ³⁴P. J. Walsh, *Phys. Rev.* **116**, 511 (1959).
- ³⁵C. M. Ferreira, J. Loureiro, and A. Ricard, *J. Appl. Phys.* **57**, 82 (1985).
- ³⁶U. Fantz, *Plasma Sources Sci. Technol.* **15**, S137 (2006).
- ³⁷U. Kortshagen and U. Bhandarkar, *Phys. Rev. E* **60**, 887 (1999).
- ³⁸V. W. Chow, D. A. Mendis, and M. Rosenberg, *J. Geophys. Res. Space Phys.* **98**, 19065, <https://doi.org/10.1029/93JA02014> (1993).
- ³⁹V. W. Chow, D. A. Mendis, and M. Rosenberg, *IEEE Trans. Plasma Sci.* **22**, 179 (1994).
- ⁴⁰M. A. Lieberman and A. J. Lichtenberg, *Principles of Plasma Discharges and Materials Processing* (Wiley, New York, 2005).
- ⁴¹L. Mangolini and U. Kortshagen, *Phys. Rev. E* **79**, 026405 (2009).
- ⁴²N. J. Kramer, R. J. Anthony, M. Mamunuru, E. S. Aydil, and U. R. Kortshagen, *J. Phys. D Appl. Phys.* **47**, 075202 (2014).
- ⁴³S. Askari, I. Levchenko, K. Ostrikov, P. Maguire, and D. Mariotti, *Appl. Phys. Lett.* **104**, 163103 (2014).
- ⁴⁴M. Kerker and E. M. Loeb, *The Scattering of Light and Other Electromagnetic Radiation* (Elsevier Science, New York, 1966).
- ⁴⁵C. F. Bohren and D. R. Huffman, *Absorption and Scattering of Light by Small Particles* (Wiley, New York, 2008).
- ⁴⁶E. D. Palik, *Handbook of Optical Constants of Solids* (Elsevier Science, New York, 1998).
- ⁴⁷B. J. Stagg and T. T. Charalampopoulos, *Combust. Flame* **94**, 381 (1993).
- ⁴⁸A. M. Malvezzi and M. Romanoni, *Int. J. Thermophys.* **13**, 131 (1992).
- ⁴⁹D. L. Greenaway, G. Harbecke, F. Bassani, and E. Tosatti, *Phys. Rev.* **178**, 1340 (1969).
- ⁵⁰H. A. Michelsen, *J. Chem. Phys.* **118**, 7012 (2003).
- ⁵¹K. S. Krishnan and S. C. Jain, *Nature* **169**, 702 (1952).
- ⁵²E. Kalered, N. Brenning, I. Pilch, L. Caillault, T. Minéa, and L. Ojamae, *Phys. Plasmas* **24**, 013702 (2017).
- ⁵³C. Kittel, *Introduction to Solid State Physics* (Wiley, New York, 2004).
- ⁵⁴H. A. Michelsen *et al.*, *Appl. Phys. B* **87**, 503 (2007).
- ⁵⁵K. McManus, J. Frank, M. Allen, and W. Rawlins, "Characterization of laser-heated soot particles using optical pyrometry," *36th AIAA Aerospace Sciences Meeting and Exhibit*, Reno, NV, 12–15 January 1998 (AIAA, Reston, VA, 1998).
- ⁵⁶H. A. Michelsen, C. Schulz, G. J. Smallwood, and S. Will, *Prog. Energy Combust. Sci.* **51**, 2 (2015).
- ⁵⁷J. V. Iribarne and B. A. Thomson, *J. Chem. Phys.* **64**, 2287 (1976).
- ⁵⁸C. J. Hogan, Jr., and J. F. de la Mora, *Phys. Chem. Chem. Phys.* **11**, 8079 (2009).
- ⁵⁹M. Gamero-Castaño and J. F. de la Mora, *J. Mass Spectrom.* **35**, 790 (2000).
- ⁶⁰See supplementary material at <http://dx.doi.org/10.1116/1.5134706> for TEM and Raman of the carbon nanoparticles utilized in this investigation.